

MIT Open Access Articles

The Influenza M2 Ectodomain Regulates the Conformational Equilibria of the Transmembrane Proton Channel: Insights from Solid-State Nuclear Magnetic Resonance

The MIT Faculty has made this article openly available. **Please share** how this access benefits you. Your story matters.

Citation: Kwon, Byungsu, and Hong, Mei. "The Influenza M2 Ectodomain Regulates the Conformational Equilibria of the Transmembrane Proton Channel: Insights from Solid-State Nuclear Magnetic Resonance." *Biochemistry* 55, 38 (September 2016): 5387–5397 © 2016 American Chemical Society

As Published: <http://dx.doi.org/10.1021/ACS.BIOCHEM.6B00727>

Publisher: American Chemical Society (ACS)

Persistent URL: <http://hdl.handle.net/1721.1/113317>

Version: Author's final manuscript: final author's manuscript post peer review, without publisher's formatting or copy editing

Terms of Use: Article is made available in accordance with the publisher's policy and may be subject to US copyright law. Please refer to the publisher's site for terms of use.





Published in final edited form as:

Biochemistry. 2016 September 27; 55(38): 5387–5397. doi:10.1021/acs.biochem.6b00727.

The Influenza M2 Ectodomain Regulates the Conformational Equilibria of the Transmembrane Proton Channel: Insights from Solid-State NMR

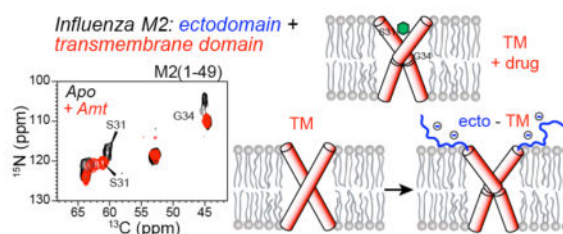
Byungsu Kwon and Mei Hong*

Department of Chemistry, Massachusetts Institute of Technology, Cambridge, Massachusetts 02139 United States

Abstract

The influenza M2 protein is the target of the amantadine family of antiviral drugs, and its transmembrane (TM) domain structure and dynamics have been extensively studied. However, little is known about the structure of the highly conserved N-terminal ectodomain, which contains epitopes targeted by influenza vaccines. In this study, we synthesized an M2 construct containing the N-terminal ectodomain and the TM domain, to understand the site-specific conformation and dynamics of the ectodomain and to investigate the ectodomain effect on the TM structure. We incorporated ^{13}C , ^{15}N -labeled residues into both domains and measured their chemical shifts and linewidths using solid-state NMR. The data indicate that the entire ectodomain is unstructured and dynamic, but the motion is slower for residues closer to the TM domain. ^{13}C lineshapes indicate that this ecto-TM construct undergoes fast uniaxial rotational diffusion, similar to the isolated TM peptide, but drug binding increases the motional rates of the TM helix while slowing down the local motion of the ectodomain residues that are close to the TM domain. Moreover, ^{13}C and ^{15}N chemical shifts indicate that the ectodomain shifts the conformational equilibria of the TM residues towards the drug-bound state even in the absence of amantadine, thus providing a molecular structural basis for the lower inhibitory concentration of full-length M2 compared to the ectodomain-truncated M2. We propose that this conformational selection may result from electrostatic repulsion between negatively charged ectodomain residues in the tetrameric protein. Together with the recent study of the M2 cytoplasmic domain, these results show that intrinsically disordered extramembrane domains in membrane proteins can regulate functionally relevant conformation and dynamics of the structurally ordered transmembrane domains.

Graphical Abstract



Introduction

The M2 protein of the influenza A virus forms a tetrameric proton channel during virus uncoating and mediates membrane scission during virus budding^{1–3}. The protein consists of three domains: an N-terminal ectodomain (roughly residues 1–21), an α -helical transmembrane (TM) domain (residues 22–46), and a cytoplasmic domain (residues 47–97)⁴. The TM domain is the core of the proton channel activity⁵, which is inhibited by the amantadine (Amt) family of antiviral drugs^{6,7}, while the cytoplasmic domain is important for virus assembly and budding⁸. The N-terminal ectodomain is highly conserved among influenza strains and mediates M2 incorporation into the virion⁹. Since mutations in the M2 TM domain have made most circulating flu viruses resistant to amantadine^{10–13}, and existing vaccines that target the highly variable hemagglutinin of seasonal flu viruses require substantial lead-time for large-scale production, there is significant interest in developing universal influenza vaccines based on the conserved M2 ectodomain^{14–17}, and M2 ectodomain-specific antibodies have been shown to bind strongly to virus-infected cells¹⁸.

Determining the structure and dynamics of the M2 ectodomain is not only important for influenza vaccine development, but also for understanding fundamental aspects of proton conduction by M2 and other ion channels. Electrophysiological measurements of full-length and truncated M2 constructs showed that ectodomain-truncated M2 variants exhibit similar proton-channel activities as the full-length protein, but have slower onset of amantadine inhibition^{5,19}. The IC₅₀ of amantadine, measured after 2 minutes of incubation with amantadine at pH 5.5, is higher (46 μ M) for the ectodomain-truncated M2(21–97) than for full-length M2 (16 μ M)¹⁹, indicating that the drug has weaker affinity for the ectodomain-truncated M2. Despite the functional roles of the two extramembrane domains, most structural studies of influenza M2 so far have excluded the ectodomain and the cytoplasmic domain beyond an amphipathic helix (AH)^{1,20,21}, and employed either TM peptide constructs or TM-AH constructs. These studies showed that the TM pore conducts protons through a mixed hydrogen-bonded chain between water molecules and the proton-selective histidine^{22–26}. Amantadine binds the N-terminal pore of the channel, at a pocket defined by residues Val27, Ala30, Ser31, and Gly34, as determined from electron densities of M2TM in detergents and from ¹³C-²H and ¹³C-¹⁵N distance experiments of M2TM in lipid bilayers^{27–30}. Drug binding dehydrates the TM pore³¹, preventing protonation of the histidine, stopping imidazole reorientation and tautomerization²⁴, thus inhibiting proton conduction. Drug binding also causes extensive chemical shift perturbation to TM residues^{32–34} and changes the TM helix orientation³⁵. NMR studies also showed that excess drug in the lipid membrane can bind to the surface of the helical bundle near Asp44^{27,36,37}, but this binding has low affinity and is not relevant to the pharmacology of amantadine inhibition^{38,39}. However, how the ectodomain affects drug binding in the TM pore, as seen in electrophysiological data, has not been investigated.

To understand the conformation and dynamics of the extramembrane domains of M2, we recently carried out a structural study of full-length M2 using 2D magic-angle-spinning (MAS) solid-state NMR (SSNMR) techniques on uniformly ¹³C, ¹⁵N-labeled protein⁴⁰. In liquid-crystalline DMPC bilayers, the protein is highly dynamic, while in gel-phase membranes, SSNMR spectra show many broad and overlapping peaks centered at random

coil chemical shifts, superimposed with α -helical chemical shifts of TM and AH-enriched hydrophobic residues. Spectral simulations strongly suggest that the conformational disorder results from the ectodomain and the cytoplasmic domain^{40, 41}. This intrinsic disorder and the associated resonance overlap precluded a more detailed study of how the ectodomain regulates the structure and dynamics of the TM helix.

In this study, we overcome this challenge by synthesizing an M2 construct that spans the ectodomain and the TM domain and incorporating site-specifically ¹³C, ¹⁵N-labeled residues. We show that the ectodomain is indeed a dynamic random coil, but the dynamics slows down towards the TM domain. Chemical shift comparison with the TM peptide indicates that the ectodomain, although unstructured, pre-organizes and shifts the TM structure towards the drug-bound conformation even in the absence of drug. The possible mechanisms of this conformational selection are discussed.

Materials and Methods

Solid-phase peptide synthesis of M2(1–18)-thioester, M2(19–49), and M2(1–49)

M2(1–49) of the influenza A/Udorn/72 strain was synthesized by Fmoc solid-phase peptide synthesis (SPPS) both with and without chemical ligation. The former involved ligating M2(1–18)-thioester and M2(19–49) through the naturally occurring Cys19. This sample contains ¹³C, ¹⁵N-labeled residues at L4, V7, I11, A30, S31, and G34 (LVIASG), and has the sequence MSLLTEVETP IRNEWGSKCN DSSDPLVVAA SIIGILHLIL WILDRLFFK. The directly synthesized peptide contains ¹³C, ¹⁵N-labeled residues at E14, G16, R18, D21, V27, A30, S31, G34, and I35 (EGRDVASGI-M2), and has the sequence MSLLTEVETP IRNEWGCRCN DSSDPLVVAA SIIGILHLIL WILDRLFFK. Thus, the ligated peptide contains SKC at residues 17–19 while the directly synthesized peptide has CRC at the corresponding positions. In total, seven residues of the ectodomain were labeled, and five TM residues were measured to compare with previous results of TM peptide constructs.

SPPS of M2(1–18) was conducted using a Lys-preloaded thioester-generating resin, H-Lys(Boc)-sulfamylbutyryl NovaSyn® TG resin. 0.1 mmol resin (0.51 g at 0.2 mmol/g loading size) was swelled for 1 hour in 2 mL *N,N*-dimethylformamide (DMF). Stepwise addition of Fmoc-protected amino acids (0.4 mmol, 4 eq.) was carried out with double coupling using 1-(Bis(dimethylamino)methylene)-1*H*-1,2,3-triazolo(4,5-*b*)pyridinium 3-oxid hexafluorophosphate (HATU) (0.4 mmol, 4 eq.) and *N,N*-diisopropylethylamine (DIPEA) (0.8 mmol, 8 eq.) in 2 mL of DMF for 0.5 – 1 h each. Fmoc cleavage was performed twice with 20% piperidine in DMF (2 mL) for 15 min and 5 min. After the last Fmoc cleavage step, the α -nitrogen of Met1 was Boc-protected by dissolving the resin-bound peptide in 0.5 mL DMF with DIPEA (1.0 mmol, 10 eq.), then adding di-*tert*-butyl dicarbonate (0.5 mmol, 5 eq.) in DMF (1.5 mL) to the solution and stirring for 2 h. After Boc protection, the resin-bound M2(1–18) was methylated at the sulfamyl group⁴². The resin-bound peptide was swelled for 2 h in 2 mL tetrahydrofuran (THF), then a 5.3 mL solution (1 : 1 v/v THF : hexane) of 1 M (trimethylsilyl)-diazomethane was added and stirred for 2 h at room temperature. Thioester formation and peptide cleavage occurred upon addition of sodium thiophenolate (0.28 mmol, 2.8 eq.) and 100-fold excess methyl 3-mercaptopropionate (28 mmol, 280 eq.). The solution was stirred at room temperature for 24 h, then filtered to

remove the cleaved resin and the filtrate containing the unbound peptide was collected and dried using a rotary evaporator.

The dry crude peptide was dissolved in 4 mL of a TFA/H₂O/TIPS/phenol mixture (88:5:2:5 v/v/v/v) and shaken for 3 h to deprotect the sidechains. The deprotected peptide was precipitated and triturated three times with cold diethyl ether. The crude peptide was re-dissolved in a 30% aqueous acetonitrile solution containing 0.1% TFA, then purified by preparative reversed-phase (RP)-HPLC using a Vydac C18 column with a linear gradient of 25–50% acetonitrile over 60 min with a flow rate of 10 mL/min and observed at 214 nm. The identity of the peaks was verified using MALDI mass spectrometry. The observed mass of 2213.91 Da was in good agreement with the calculated mass of 2212.52 Da. The synthesis and purification yield of M2(1–18)-thioester was 15%.

M2(19–49) was synthesized on a rink amide MBHA resin. 0.07 mmol resin (0.087 g with a 0.79 mmol/g loading size) was swelled for 2 h in 2 mL DMF and activated by cleaving the terminal Fmoc group using 2 × 2 mL of 20% piperidine in DMF. After the last coupling step, the peptide was deprotected and cleaved from the resin by addition of 4 mL TFA/H₂O/TIPS/phenol solution (88:5:2:5 by volume) for 2 h. The resin was filtered off, and the crude peptide was precipitated and triturated three times with cold diethyl ether and dissolved in 60% acetonitrile solution containing 0.1% TFA. Crude peptide was purified by preparative RP-HPLC using a Vydac C18 column with a linear gradient of 80–99% acetonitrile over 60 min at a flow rate of 10 mL/min. MALDI-MS analysis showed a mass of 3494.53 Da, in good agreement with the calculated mass of 3493.15 Da. The yield of M2(19–49) was 8%.

Direct synthesis of M2(1–49) was conducted on an H-Rink amide ChemMatrix[®] resin. 0.05 mmol resin (0.1 g with a 0.4–0.6 mmol/g loading size) was swelled for 2 h in 2 mL DMF. After the last coupling step, the peptide was deprotected and cleaved from the resin by addition of TFA/Phenol/H₂O/TIPS solution (88 : 5 : 5 : 2 by volume) for 3 h. The resin was filtered off, and the crude peptide was precipitated and triturated three times with cold diethyl ether and dissolved in 50% acetonitrile solution containing 0.1% TFA. Crude peptide was purified by preparative RP-HPLC using a Vydac C4 column with a linear gradient of 50–99% acetonitrile over 120 min at a flow rate of 10 mL/min. MALDI-MS analysis gave a mass of 5646.11 Da, in excellent agreement with the calculated mass of 5646.58 Da. The total synthesis and purification yield of M2(1–49) was ~5%.

Native chemical ligation of M2(1–49)

M2(1–18) thioester and M2(19–49) were ligated by adding 50% molar excess of 25.8 mM M2(19–49) in 0.1 mL of 60% TFE (v/v) solution to 1.6 mM M2(1–18)-thioester in 2.5 mL of ligation buffer. The ligation buffer consists of 60% TFE (v/v), 5.2 M guanidine hydrochloride, 96 mM sodium phosphate, 50 mM 4-mercapto-phenylacetic acid (MPAA) and 20 mM Tris(2-carboxyethyl)phosphine (TCEP) hydrochloride. The pH 4.5 solution was stirred at 35°C, then the reaction was initiated by increasing the pH to 7.0 using concentrated NaOH. The reaction was monitored by analytical RP-HPLC using a Vydac C4 column (5 µm particle size, 0.46 cm × 15 cm) with a 40–99% acetonitrile gradient over 30 min at a flow rate of 2 mL/min. Unreacted M2(1–18)-thioester and M2(19–49) peptides appeared at 1.6 min and 19.0 min, respectively, while the ligation product appeared at 16.5 min. The

ligation was complete after 6 hours. M2(1–49) was purified by preparative RP-HPLC using a linear gradient of 70–99% acetonitrile over 60 min at a flow rate of 13 mL/min and the mass was confirmed by MALDI-MS. The observed mass of 5587.93 Da is in good agreement with the calculated mass of 5585.50 Da. About 4.6 mg of purified ligation product was obtained from starting amounts of ~9 mg each of the two peptide segments, corresponding to a ligation yield of ~32% based on the limiting reagent, M2(19–49).

Membrane reconstitution of M2(1–49)

M2(1–49) peptides were reconstituted into DMPC bilayers by organic-phase mixing. About 2 mg and 4 mg of LVIASG- and EGRDVASGI-labeled peptides in 300 μ L TFE were mixed with 6 mg and 12 mg of DMPC in 300 μ L chloroform, respectively. The peptide : lipid molar ratio (P : L) was 1 : 25. The organic solvents were removed with a stream of nitrogen gas and the mixture was lyophilized overnight. The protein-lipid mixture was suspended in pH 7.5 Tris buffer (10 mM Tris base, 1 mM ethylenediaminetetraacetic acid, and 1 mM sodium azide) freeze-thawed between liquid-nitrogen temperature and 30°C five times, followed by bath sonication for ~4 min. The proteoliposome solution was centrifuged at 40,000 rpm at 4°C for 6 hours to obtain a membrane pellet. With this preparation, the peptide is homogeneously mixed in multilamellar DMPC vesicles. The pellet was equilibrated to a hydration level of ~40% by mass, packed into a 3.2 mm MAS rotor and stored at –30°C until the solid-state NMR experiments. For amantadine-bound samples, the drug was titrated into the membrane pellet at a drug : tetramer molar ratio of 4 : 1. This molar ratio is in moderate excess of the stoichiometric ratio of 1 drug per tetramer, to ensure saturations of all channels and to allow comparison with previous TM peptide data measured under 4 : 1 or 5 : 1 drug : tetramer ratios^{27, 36}. This organic-phase membrane reconstitution method produces the same equilibrium structures, oligomeric states, and dynamics as aqueous-phase mixing based on detergent dialysis, as shown by measurements on the M2 TM peptide^{32, 33, 43} and various antimicrobial peptides^{44–47}.

Solid-state NMR experiments

Solid-state NMR spectra were measured on a 900 MHz (21.1 Tesla) Bruker NMR spectrometer using a 3.2 mm $^1\text{H}/^{13}\text{C}/^{15}\text{N}$ MAS probe. Typical radiofrequency field strengths were 71 kHz, 63 kHz, and 42 kHz for ^1H , ^{13}C , and ^{15}N pulses, respectively. Spectra were measured in both gel-phase and liquid-crystalline membranes to investigate both the conformation and dynamics of the protein. ^{13}C chemical shifts were externally referenced to the CH_2 signal of adamantane at 38.48 ppm on the TMS scale and ^{15}N chemical shifts were referenced to the ^{15}N signal of N-acetylvaline at 122.0 ppm on the liquid ammonia scale. 2D ^{13}C - ^{13}C correlation spectra were measured using a dipolar-assisted rotational resonance (DARR) experiment⁴⁸ to obtain ^{13}C chemical shifts. 2D ^{15}N - ^{13}C correlation spectra were measured at 263 K under 12 kHz MAS using a REDOR pulse train for ^{13}C - ^{15}N polarization transfer⁴⁹. We also measured ^{13}C J-INADEQUATE spectra of M2(1–49) using direct ^{13}C polarization^{50–52} to obtain the chemical shifts of mobile residues. The experiment was carried out on DMPC-bound M2(1–49) at 303 K under 12 kHz.

Results

Native chemical ligation and direct synthesis of M2(1–49) both gave sufficiently high yields to allow the incorporation of ^{13}C , ^{15}N -labeled residues from L4 to D21 into the ectodomain, thus giving comprehensive information about the ectodomain conformation and dynamics. In addition, key TM residues were labeled to monitor the TM helix conformation in the presence of the ectodomain. We chose DMPC to reconstitute M2(1–49), because DMPC has been used in SSNMR studies of all M2 constructs so far, including the TM peptide ^{43, 53}, the intermediate TM-AH construct ⁵⁴, and the full-length protein ^{40, 41}, thus this membrane allows comparison of the conformation of the ecto-TM M2 with the other constructs. In addition, the influenza M2 protein is known to be structurally plastic under different environmental conditions, including pH, drug binding, membrane thickness, membrane curvature, and membrane surface charge ^{21, 55, 56}. Extensive NMR data have shown that the DMPC bilayer supports the full panel of M2 functions, including drug binding, pH-induced conformational changes, and curvature induction by the amphipathic helix. Alternative lipid membranes such as DOPC/DOPE ²⁶, diphytanoylphosphocholine ⁵⁷, and cholesterol- and sphingomyelin-containing membranes ⁵⁸ have either not been used for all M2 construct lengths or can produce structural features that are not fully consistent with all the M2 functions.

Fig. 1 shows 1D ^{13}C DP spectra and 2D ^{13}C - ^{13}C correlation spectra of M2(1–49) in DMPC bilayers. At high temperature, the ectodomain residues show narrow peaks with random coil $\text{C}\alpha$ and $\text{C}\beta$ chemical shifts. Residues L4, V7, and I11 have narrower linewidths (0.3–0.5 ppm) than residues E14, G16, R18, D21 (~1.0 ppm), indicating that the N-terminal residues are more mobile than TM-proximal residues. The 2D J-INADEQUATE spectrum and DARR spectrum confirmed the high mobility of the ectodomain and fully resolved the chemical shifts (Table 1), while TM signals are absent in these spectra, indicating the relative rigidity of the TM domain. Thus, the ectodomain is unstructured and has a decreasing motional gradient towards the TM domain. This mobility gradient is shown more quantitatively in the ^{13}C linewidths plotted as a function of residue position (Fig. 1e): the linewidths increase from the N-terminus of the ectodomain to the C-terminus, and increase further to 0.8–1.8 ppm for TM residues (*vide infra*).

Fig. 2 compares 1D ^{13}C cross-polarization (CP) and direct-polarization (DP) spectra of M2(1–49) in the absence and presence of amantadine. ^{13}C CP spectra preferentially detect rigid residues while DP spectra preferentially detect mobile residues. At 303 K, all TM residues show broad signals in the absence of the drug, but the peaks narrow substantially upon drug binding. Decreasing the temperature to 263 K reduced this linewidth contrast between the apo and drug-bound states, because the apo peptide now also exhibits relatively narrow lines. These spectra indicate that the broad linewidths of the apo M2(1–49) at high temperature results from intermediate timescale motion, which is most likely uniaxial rotational diffusion of the entire helix bundle, and drug binding speeds up this motion, thus narrowing the linewidths. This dynamics is very similar to that observed in the TM peptide ^{20, 33, 43, 58, 59}, indicating that the ectodomain does not inhibit rotational diffusion of the four-helix bundle. In comparison, for the ectodomain, E14, R18 and D21 signals exhibit the opposite change of increasing linewidths upon drug binding (Fig. 2c). For example, the

E14 sidechain C δ , R18 C δ and D21 C γ peaks decreased in intensity, while the G16 C α signal became undetectable in the drug-bound sample. For residues L4, V7 and I11 near the N-terminus, the linewidths are largely unperturbed by drug binding (Fig. 2d). Thus, amantadine binding slows down the local motions of the random coil near the TM domain while leaving the N-terminus of the ectodomain unaffected.

To investigate the effects of the ectodomain on the drug binding property of the TM helix, we measured 2D ^{15}N - ^{13}C (Fig. 3) and ^{13}C - ^{13}C (Fig. 4) correlation spectra of M2(1–49) at 263 K in gel-phase DMPC. At this temperature, the TM domain is immobilized, and all TM residues show α -helical chemical shifts, but the chemical shifts show interesting differences from those of the TM peptide (Table 2). First, S31 in apo M2(1–49) exhibits an ^{15}N chemical shift of 118 ppm, which is intermediate between the drug-bound chemical shift of 120 ppm and the apo chemical shift of 114 ppm found in M2(22–46) (Fig. 3b). Consistently, while the drug-bound TM peptide has residual intensities at the unbound S31 ^{15}N chemical shift of 114 ppm, in drug-bound M2(1–49) the S31 ^{15}N chemical shift is fully moved to 120 ppm. Thus, the ectodomain shifts the S31 conformational equilibrium towards the drug-bound state. For G34, apo M2(1–49) displays two peaks with ^{15}N chemical shifts of 105 and 110 ppm with an intensity ratio of 1 : 2 in the ^{15}N - ^{13}C correlation spectrum. Drug binding quantitatively converted all intensities to the 110-ppm peak. Thus, G34 in apo M2(1–49) already samples the drug-bound conformation. In comparison, the TM peptide partly retains the ^{15}N chemical shift of 107 ppm even in the drug-bound sample (Fig. 3a). To compare the effects of the ectodomain and drug binding on the TM conformation, we plot three types of chemical shift differences in Fig. 3e: between the apo and drug-bound states for M2(1–49); between the apo and drug-bound states for the TM peptide M2(22–46); and between the short and long peptides in the absence of drug. The bar diagram shows that the presence of the ectodomain significantly reduces the chemical shift difference between the apo and drug-bound states for residues in the drug-binding pocket of A30 to I35.

In addition to the ectodomain-induced and drug-induced chemical shift changes, 2D ^{13}C - ^{13}C correlation spectra (Fig. 5) show multiple inter-residue cross peaks at 500 ms spin diffusion mixing. Sequential A30–S31 and G34–I35 cross peaks are observed, which are already present at 100 ms (Fig. 4). In addition, we observed three-, four-, and five-residue correlation peaks of V27–A30, V27–S31, S31–G34, S31–I35, and A30–I35. The i to $i+4$ and i to $i+3$ residue pairs are close in space within the same α -helix, as confirmed by the 1.65 Å crystal structure of M2(25–46) (PDB:3LBW)⁶⁰. For example, the i to $i+4$ V27 α –S31 α and S31 α –I35 α distances are 6.0 Å and 6.5 Å, while the i to $i+3$ V27 α –A30 α and S31 α –G34 α distances are 5.1 Å and 5.2 Å, respectively. These inter-residue distances are much shorter in the same helix than between different helices. In comparison, the observed A30C α –I35C α cross peak is most likely intermolecular, since the intramolecular distance of ~8.6 Å is longer than the nearest-neighbor inter-helical distance of 6.0 Å (Fig. 5b).

Discussion

The purpose of this study is two-fold: to obtain site-specific conformational constraints of the M2 ectodomain and to investigate its influences on the TM helix structure. The ectodomain is highly conserved among influenza A viruses and is a target of universal

influenza vaccines. In the current study, we adopted the chemical approach of synthesizing an ecto-TM construct to enable site-specific studies of the ectodomain and TM structure and dynamics. The presence of a naturally occurring Cys19 allowed us to employ native chemical ligation to produce M2(1–49). But even direct synthesis of the full 49-residue protein proved to be feasible because of the highly polar nature of the ectodomain. With the synthetic accessibility of this ecto-TM construct, we are able to incorporate a number of ^{13}C , ^{15}N -labeled residues into the ectodomain and at key TM sites.

^{13}C chemical shifts (Fig. 1, 2) unambiguously indicate that the entire ectodomain is intrinsically disordered, thus confirming the structural prediction from previous spectral simulations⁴⁰. However, the ectodomain dynamics is not uniform: residues closer to the TM domain such as R18 and D21 have broader linewidths and hence slower motions than residues near the N-terminus such as L4 and V7. This mobility gradient is not surprising, and may result from two factors: the TM domain may tether and partially immobilize the neighboring ectodomain residues, and proximity to lipid headgroups on the membrane surface may also partly immobilize ectodomain residues that are close to the TM domain.

Drug binding slowed down the mobility of ectodomain residues close to the TM domain, as seen by increased linewidths of residues E14 to D21 in the drug-bound state compared to the apo state, while the linewidths of **residues L4, V7 and I11 are unaffected by drug binding** (Fig. 2c, d). These behaviors differ from those of the TM residues, which exhibit line narrowing upon drug binding. The different dynamic responses of the ectodomain and the TM domain to drug binding result from their different motions: the ectodomain mainly undergoes random segmental motions while the TM four-helix bundle mainly undergoes correlated rotational diffusion²⁰. In TM peptide samples, temperature-dependent $T_{1\rho}$ relaxation NMR data showed that the drug speeds up the uniaxial rotational diffusion^{32, 61}. The average motional correlation times at 313 K decreased from 2.8 μs to 0.9 μs by drug binding, while the activation energy of the rotational diffusion increased from 14 to 23 kJ/mol. This accelerated diffusion was attributed to the formation of a tighter helical bundle in the presence of the drug. The same linewidth changes for the TM residues in M2(1–49) indicate that the uniaxial diffusion is similarly *accelerated* by the drug. Thus, amantadine tightens the four-helix bundle in the presence of the ectodomain, which should cause the C-terminal half of the ectodomain to approach each other, thus slowing down its local motions.

2D correlation spectra indicate that the ectodomain changes the chemical shifts of the TM residues in the same direction as drug-induced chemical shift changes. This is most clearly seen at S31 and G34, where the S31 ^{15}N chemical shift in apo M2(1–49) approaches the value in drug-bound M2(22–46), and G34 in apo M2(1–49) shows both unbound and bound chemical shifts even though the drug is absent. The larger ^{15}N chemical shift of G34 has been assigned to a kinked-helix conformation based on ^{15}N - ^1H dipolar coupling measurements on oriented TM peptides in DMPC bilayers (PDB accession code: 2H95)³⁵. We attribute the S31 conformation with the larger ^{15}N chemical shift to (ϕ, ψ) torsion angles that give rise to a more spacious pore at this position to accommodate the drug. Overall, these chemical shift changes indicate that the ectodomain selects the drug-bound conformation of the TM helix even in the absence of the drug. This conformational pre-organization is consistent with, and provides a molecular structure corollary, to the weaker

affinity of amantadine for ectodomain-truncated M2(21–97) than for full-length M2, as manifested by 3-fold higher IC_{50} for the truncation mutant¹⁹. Since the ectodomain lies at the path of drug entry to the TM pore, it may be counterintuitive that the ectodomain should facilitate drug binding. We propose that electrostatic repulsion between the ectodomain random coils may enlarge the drug-binding site. The ectodomain contains four acidic Glu and Asp residues and only two cationic residues. Thus, at neutral pH, this domain carries a net charge of -2 . The resulting electrostatic repulsion may increase the tilt angle of the N-terminal half of the TM helix, thus promoting a similar conformation as the drug-bound state of the TM peptide. Fig. 6 depicts the effects of drug binding versus the ectodomain on the conformational equilibrium of the TM helix bundle. Both factors should shift the TM structure towards the kinked conformation at G34 and a larger pore diameter at S31. The synergistic effect of the ectodomain and drug binding is consistent with the observed interhelical A30–I35 cross peaks, which indicate a well-packed four-helix bundle, since amantadine has been shown to tighten the four-helix bundle formed by the TM peptide⁶¹.

A second possible factor for ectodomain's selection of the drug-bound conformation of the TM helix is the role of two conserved cysteines at C17 and C19. Sucrose gradient analysis and chemical cross-linking experiments⁶² showed that both cysteines can form intermolecular disulfide bonds under non-reducing conditions: the double-cysteine wild-type sequence forms disulfide-linked tetramers while single Cys-to-Ser mutations at either position promotes a pair of non-covalently associated disulfide-bonded dimers. Thus, these two cysteines can affect the symmetry and conformation of the tetramer. In the current study, the directly synthesized EGRDVASGI-M2(1–49) contains both C17 and C19 while the ligated LVIASG-M2(1–49) peptide contains S17 and C19. If the disulfide bonds found in detergents under non-reducing conditions persist in DMPC bilayers under our experimental conditions, then the EGRDVASGI-M2 sample would be expected to form disulfide-bonded symmetric tetramers while the LVIASG-M2 sample would be expected to form a dimer of dimer. However, both apo M2(1–49) samples exhibit S31 and G34 chemical shifts that approach the drug-bound chemical shifts of the TM peptide, despite their different disulfide-forming abilities. This suggests that intermolecular disulfide bonds may not be the chief reason for the conformational selection. Additional experiments will be necessary to determine whether the tetramers are indeed disulfide-linked in lipid bilayers and to elucidate the influence of the two cysteines on the TM conformational equilibrium.

The influence of the random-coil ectodomain on the drug-binding equilibrium of the TM helix has interesting parallels with the influence of the unstructured cytoplasmic tail on the proton-conduction equilibria of His37. Our recent study of the TM- and cytoplasmic-containing M2(21–97) found that proton shuttling by His37 occurs at higher pH than in TM peptide constructs⁴¹. Moreover, M2(21–97) exhibits additional His37 cross peaks at chemical shifts that correspond to more ideal α -helical conformations, which are absent in TM peptide samples. The higher pK_a 's and more ideal helical conformations suggest that the unstructured cytoplasmic tail beyond the amphipathic helix, which contains many acidic Glu and Asp residues, may increase the tilt angle of the C-terminal half of the TM helix due to electrostatic repulsion, thus reducing the energy barrier for proton binding to the His37 tetrad. Taken together, these results suggest a consistent theme where the N-terminal ectodomain and the C-terminal post-AH cytoplasmic tail, despite their unstructured nature,

regulate the TM conformational equilibria to promote the drug-sensitive proton-channel function. The ectodomain shifts the drug-binding equilibria of the TM helix towards the bound state, while the post-AH cytoplasmic tail shifts the proton-binding equilibria of the TM helix in favor of proton binding. Future experiments will probe whether the ectodomain also regulates the His37 proton-conduction equilibria while the cytoplasmic domain may also modulate the drug-binding equilibria.

The unstructured nature of the ectodomain and the cytoplasmic domain has implications for understanding M2 interactions with other influenza virus proteins and with antibodies. For example, Ile11 and Glu14 are the epitopes for 14C2 monoclonal antibodies (mAbs)^{63, 64} while Ser2, Thr5, and Glu6 are involved in binding anti-M2 ectodomain mAbs¹⁶. Recently, two crystal structures of M2 ectodomain fragments bound to two different antibodies were reported^{65, 66}. Other than a common β -turn in the N-terminal half of the ectodomain, the structures differ in many details. This is consistent with the highly dynamic nature of the unbound ectodomain seen here, since this mobility primes the ectodomain for macromolecular recognition.

Acknowledgments

Funding Information

This work is funded by NIH grant GM088204 to M.H. The 900 MHz spectra were measured at the MIT/Harvard Center for Magnetic Resonance, which is supported by NIH grant EB002026.

References

1. Hong M, DeGrado WF. Structural basis for proton conduction and inhibition by the influenza M2 protein. *Protein Sci.* 2012; 21:1620–1633. [PubMed: 23001990]
2. Pinto LH, Lamb RA. The M2 Proton Channels of Influenza A and B Viruses. *J Biol Chem.* 2006; 281:8997–9000. [PubMed: 16407184]
3. Rossman JS, Lamb RA. Influenza virus assembly and budding. *Virology.* 2011; 411:229–236. [PubMed: 21237476]
4. Lamb, RA., Holsinger, KJ., Pinto, LH. The Influenza A virus M2 ion channel protein and its role in the influenza virus life cycle. In: Wemmer, E., editor. *Cellular Receptors of Animal Viruses*. Cold Spring Harbor Lab Press; Plainview, NY: 1994. p. 303-321.
5. Ma C, Polishchuk AL, Ohigashi Y, Stouffer AL, Schön A, Magavern E, Jing X, Lear JD, Freire E, Lamb RA, DeGrado WF, Pinto LH. Identification of the Functional Core of the Influenza A Virus A/M2 Proton-Selective Ion Channel. *Proc Natl Acad Sci USA.* 2009; 106:12283–12288. [PubMed: 19590009]
6. Hay AJ, Wolstenholme AJ, Skehel JJ, Smith MH. The molecular basis of the specific anti-influenza action of amantadine. *EMBO J.* 1985; 4:3021–3024. [PubMed: 4065098]
7. Wang C, Takeuchi K, Pinto LH, Lamb RA. Ion channel activity of influenza A virus M2 protein: characterization of the amantadine block. *J Virol.* 1993; 67:5585–5594. [PubMed: 7688826]
8. McCown MF, Pekosz A. Distinct domains of the influenza A virus M2 protein cytoplasmic tail mediate binding to the M1 protein and facilitate infectious virus production. *J Virol.* 2006; 80:8178–8189. [PubMed: 16873274]
9. Park EK, Castrucci MR, Portner A, Kawaoka Y. The M2 ectodomain is important for its incorporation into influenza A virions. *J Virol.* 1998; 72:2449–2455. [PubMed: 9499106]
10. Bright RA, Shay DK, Shu B, Cox NJ, Klimov AI. Adamantane resistance among influenza A viruses isolated early during the 2005–2006 influenza season in the United States. *JAMA.* 2006; 295:891–894. [PubMed: 16456087]

11. Wang J, Cady SD, Balannik V, Pinto LH, DeGrado WF, Hong M. Discovery of spiro-piperidine inhibitors and their modulation of the dynamics of the M2 proton channel from influenza A virus. *J Am Chem Soc.* 2009; 131:8066–8076. [PubMed: 19469531]
12. Wang J, Ma C, Fiorin G, Carnevale V, Wang T, Hu F, Lamb RA, Pinto LH, Hong M, Klein ML, DeGrado WF. Molecular dynamics simulation directed rational design of inhibitors targeting drug-resistant mutants of influenza A virus M2. *J Am Chem Soc.* 2011; 133:12834–12841. [PubMed: 21744829]
13. Dong J, Chen S, Li R, Cui W, Jiang H, Ling Y, Yang Z, Hu W. Imidazole-based pinanamine derivatives: Discovery of dual inhibitors of the wild-type and drug-resistant mutant of the influenza A virus. *Eur J Med Chem.* 2016; 108:605–615. [PubMed: 26722757]
14. De Filette M, Jou WM, Birkett A, Lyons K, Schultz B, Tonkyro A, Resch S, Fiers W. Universal influenza A vaccine: Optimization of M2-based constructs. *Virology.* 2005; 337:149–161. [PubMed: 15914228]
15. Deng L, Cho KJ, Fiers W, Saelens X. M2e-Based Universal Influenza A Vaccines. *Vaccine.* 2015; 3:105–136.
16. Grandea AG, Olsen OA, Cox TC, Renshaw M, Hammond PW, Chan-Hui PY, Mitcham JL, Cieplak W, Stewart SM, Grantham ML, Pekosz A, Kiso M, Shinya K, Hatta M, Kawaoka Y, Moyle M. Human antibodies reveal a protective epitope that is highly conserved among human and nonhuman influenza A viruses. *Proc Natl Acad Sci USA.* 2010; 107:12658–12663. [PubMed: 20615945]
17. Rappazzo CG, Watkins HC, Guarino CM, Chau A, Lopez JL, DeLisa MP, Leifer CA, Whittaker GR, Putnam D. Recombinant M2e outer membrane vesicle vaccines protect against lethal influenza A challenge in BALB/c mice. *Vaccine.* 2016; 34:1252–1258. [PubMed: 26827663]
18. Mozdzanowska K, Feng JQ, Eid M, Kragol G, Cudic M, Otvos L, Gerhard W. Induction of influenza type A virus-specific resistance by immunization of mice with a synthetic multiple antigenic peptide vaccine that contains ectodomains of matrix protein 2. *Vaccine.* 2003; 21:2616–2626. [PubMed: 12744898]
19. Ohigashi Y, Ma C, Jing X, Balannick V, Pinto LH, Lamb RA. An amantadine-sensitive chimeric BM2 ion channel of influenza B virus has implications for the mechanism of drug inhibition. *Proc Natl Acad Sci U S A.* 2009; 106:18775–18779. [PubMed: 19841275]
20. Cady SD, Luo WB, Hu FH, Hong M. Structure and Function of the Influenza A M2 Proton Channel. *Biochemistry.* 2009; 48:7356–7364. [PubMed: 19601584]
21. Zhou HX, Cross TA. Influences of membrane mimetic environments on membrane protein structures. *Annu Rev Biophys.* 2013; 42:361–392. [PubMed: 23451886]
22. Wang C, Lamb RA, Pinto LH. Activation of the M(2) Ion-Channel of Influenza-Virus - a Role for the Transmembrane Domain Histidine Residue. *Biophys J.* 1995; 69:1363–1371. [PubMed: 8534806]
23. Pinto LH, Dieckmann GR, Gandhi CS, Papworth CG, Braman J, Shaughnessy MA, Lear JD, Lamb RA, DeGrado WF. A functionally defined model for the M-2 proton channel of influenza A virus suggests a mechanism for its ion selectivity. *Proc Natl Acad Sci USA.* 1997; 94:11301–11306. [PubMed: 9326604]
24. Hu F, Luo W, Hong M. Mechanisms of proton conduction and gating by influenza M2 proton channels from solid-state NMR. *Science.* 2010; 330:505–508. [PubMed: 20966251]
25. Hu F, Schmidt-Rohr K, Hong M. NMR detection of pH-dependent histidine-water proton exchange reveals the conduction mechanism of a transmembrane proton channel. *J Am Chem Soc.* 2012; 134:3703–3713. [PubMed: 21974716]
26. Sharma M, Yi M, Dong H, Qin H, Peterson E, Busath D, Zhou HX, Cross TA. Insight into the mechanism of the influenza A proton channel from a structure in a lipid bilayer. *Science.* 2010; 330:509–512. [PubMed: 20966252]
27. Cady SD, Schmidt-Rohr K, Wang J, Soto CS, Degrado WF, Hong M. Structure of the amantadine binding site of influenza M2 proton channels in lipid bilayers. *Nature.* 2010; 463:689–692. [PubMed: 20130653]

28. Stouffer AL, Acharya R, Salom D, Levine AS, Di Costanzo L, Soto CS, Tereshko V, Nanda V, Stayrook S, DeGrado WF. Structural basis for the function and inhibition of an influenza virus proton channel. *Nature*. 2008; 451:596–599. [PubMed: 18235504]
29. Wang J, Qiu JX, Soto CS, DeGrado WF. Structural and dynamic mechanisms for the function and inhibition of the M2 proton channel from influenza A virus. *Curr Opin Struct Biol*. 2011; 21:68–80. [PubMed: 21247754]
30. Andreas LB, Barnes AB, Corzilius B, Chou JJ, Miller EA, Caporini M, Rosay M, Griffin RG. Dynamic nuclear polarization study of inhibitor binding to the M2(18–60) proton transporter from influenza A. *Biochemistry*. 2013; 52:2774–2782. [PubMed: 23480101]
31. Luo W, Hong M. Conformational changes of an ion channel membrane protein detected through water-protein interactions using solid-state NMR spectroscopy. *J Am Chem Soc*. 2010; 132:2378–2384. [PubMed: 20112896]
32. Cady SD, Hong M. Amantadine-Induced Conformational and Dynamical Changes of the Influenza M2 Transmembrane Proton Channel. *Proc Natl Acad Sci USA*. 2008; 105:1483–1488. [PubMed: 18230730]
33. Cady SD, Mishanina TV, Hong M. Structure of Amantadine-Bound M2 Transmembrane Peptide of Influenza A in Lipid Bilayers from Magic-Angle-Spinning Solid-State NMR: The Role of Ser31 in Amantadine Binding. *J Mol Biol*. 2009; 385:1127–1141. [PubMed: 19061899]
34. Andreas LB, Eddy MT, Pielak RM, Chou JJ, Griffin RG. Magic angle spinning NMR investigation of influenza A M2(18–60): support for an allosteric mechanism of inhibition. *J Am Chem Soc*. 2010; 132:10958–10960. [PubMed: 20698642]
35. Hu J, Asbury T, Achuthan S, Li CG, Bertram R, Quine JR, Fu RQ, Cross TA. Backbone structure of the amantadine-blocked trans-membrane domain M2 proton channel from influenza A virus. *Biophys J*. 2007; 92:4335–4343. [PubMed: 17384070]
36. Cady SD, Wang J, Wu YB, DeGrado WF, Hong M. Specific Binding of Adamantane Drugs and Direction of Their Polar Amines in the Pore of the Influenza M2 Transmembrane Domain in Lipid Bilayers and Dodecylphosphocholine Micelles Determined by NMR Spectroscopy. *J Am Chem Soc*. 2011; 133:4274–4284. [PubMed: 21381693]
37. Schnell JR, Chou JJ. Structure and mechanism of the M2 proton channel of influenza A virus. *Nature*. 2008; 451:591–595. [PubMed: 18235503]
38. Jing XH, Ma CL, Ohigashi Y, Oliveira FA, Jardetzky TS, Pinto LH, Lamb RA. Functional studies indicate amantadine binds to the pore of the influenza A virus M2 proton-selective ion channel. *Proc Natl Acad Sci USA*. 2008; 105:10967–10972. [PubMed: 18669647]
39. Pielak RM, Oxenoid K, Chou JJ. Structural investigation of rimantadine inhibition of the AM2–BM2 chimera channel of influenza viruses. *Structure*. 2011; 19:1655–1663. [PubMed: 22078564]
40. Liao SY, Fritzsche KJ, Hong M. Conformational analysis of the full-length M2 protein of the influenza A virus using solid-state NMR. *Protein Sci*. 2013; 22:1623–1638. [PubMed: 24023039]
41. Liao SY, Yang Y, Tietze D, Hong M. The Influenza M2 Cytoplasmic Tail Changes the Proton-Exchange Equilibria and the Backbone Conformation of the Transmembrane Histidine Residue to Facilitate Proton Conduction. *J Am Chem Soc*. 2015; 137:6067–6077. [PubMed: 25892574]
42. Kwon B, Tietze D, White PB, Liao SY, Hong M. Chemical ligation of the influenza M2 protein for solid-state NMR characterization of the cytoplasmic domain. *Protein Sci*. 2015; 24:1087–1099. [PubMed: 25966817]
43. Cady SD, Goodman C, Tatko CD, DeGrado WF, Hong M. Determining the orientation of uniaxially rotating membrane proteins using unoriented samples: A (2)H, (13)C, and (15)N solid-state NMR investigation of the dynamics and orientation of a transmembrane helical bundle. *J Am Chem Soc*. 2007; 129:5719–5729. [PubMed: 17417850]
44. Buffy JJ, Waring AJ, Lehrer RI, Hong M. Immobilization and Aggregation of Antimicrobial Peptide Protegrin in Lipid Bilayers Investigated by Solid-State NMR. *Biochemistry*. 2003; 42:13725–13734. [PubMed: 14622019]
45. Mani R, Tang M, Wu X, Buffy JJ, Waring AJ, Sherman MA, Hong M. Membrane-bound dimer structure of a b-hairpin antimicrobial peptide from rotational-echo double-resonance solid-state NMR. *Biochemistry*. 2006; 45:8341–8349. [PubMed: 16819833]

46. Tang M, Waring AJ, Hong M. Phosphate-Mediated Arginine Insertion Into Lipid Membranes and Pore Formation by a Cationic Membrane Peptide from Solid-State NMR. *J Am Chem Soc.* 2007; 129:11438–11446. [PubMed: 17705480]
47. Tang M, Waring AJ, Lehrer RI, Hong M. Effects of Guanidinium-Phosphate Hydrogen Bonding on the Membrane-Bound Structure and Activity of an Arginine-Rich Membrane Peptide from Solid-State NMR. *Angew Chem Int Ed Engl.* 2008; 47:3202–3205. [PubMed: 18338418]
48. Takegoshi K, Nakamura S, Terao T. C-13-H-1 dipolar-assisted rotational resonance in magic-angle spinning NMR. *Chem Phys Lett.* 2001; 344:631–637.
49. Hong M, Griffin RG. Resonance Assignment for Solid Peptides by Dipolar-Mediated ¹³C/¹⁵N Correlation Solid-State NMR. *J Am Chem Soc.* 1998; 120:7113–7114.
50. Lesage A, Auger C, Caldarelli S, Emsley L. Determination of through-bond carbon-carbon connectivities in solid-state NMR using the INADEQUATE experiment. *J Am Chem Soc.* 1997; 119:7867–7868.
51. Lesage A, Bardet M, Emsley L. Through-bond carbon-carbon connectivities in disordered solids by NMR. *J Am Chem Soc.* 1999; 121:10987–10993.
52. Hong M. Solid-state dipolar INADEQUATE NMR spectroscopy with a large double-quantum spectral width. *J Magn Reson.* 1999; 136:86–91. [PubMed: 9887293]
53. Wang JF, Kim S, Kovacs F, Cross TA. Structure of the transmembrane region of the M2 protein H⁺ channel. *Protein Sci.* 2001; 10:2241–2250. [PubMed: 11604531]
54. Wang T, Hong M. Investigation of the Curvature Induction and Membrane Localization of the Influenza Virus M2 Protein Using Static and Off-Magic-Angle-Spinning Solid-State Nuclear Magnetic Resonance of Oriented Bicelles. *Biochemistry.* 2015; 54:2214–2226. [PubMed: 25774685]
55. Li C, Qin H, Gao FP, Cross TA. Solid-state NMR characterization of conformational plasticity within the transmembrane domain of the influenza A M2 proton channel. *Biochim Biophys Acta.* 2007; 1768:3162–3170. [PubMed: 17936720]
56. Hu FH, Luo WB, Cady SD, Hong M. Conformational plasticity of the influenza A M2 transmembrane helix in lipid bilayers under varying pH, drug binding, and membrane thickness. *BBA-Biomembranes.* 2011; 1808:415–423. [PubMed: 20883664]
57. Andreas LB, Reese M, Eddy MT, Gelev V, Ni QZ, Miller EA, Emsley L, Pintacuda G, Chou JJ, Griffin RG. Structure and Mechanism of the Influenza A M218–60 Dimer of Dimers. *J Am Chem Soc.* 2015; 137:14877–14886. [PubMed: 26218479]
58. Luo WB, Cady SD, Hong M. Immobilization of the Influenza A M2 Transmembrane Peptide in Virus Envelope-Mimetic Lipid Membranes: A Solid-State NMR Investigation. *Biochemistry.* 2009; 48:6361–6368. [PubMed: 19489611]
59. Cady SD, Hong M. Simultaneous extraction of multiple orientational constraints of membrane proteins by C-13-detected N-H dipolar couplings under magic angle spinning. *J Magn Reson.* 2008; 191:219–225. [PubMed: 18221902]
60. Acharya A, Carnevale V, Fiorin G, Levine BG, Polishchuk A, Balannick V, Samish I, Lamb RA, Pinto LH, DeGrado WF, Klein ML. Structural mechanism of proton transport through the influenza A M2 protein. *Proc Natl Acad Sci U S A.* 2010; 107:15075–15080. [PubMed: 20689043]
61. Cady SD, Hong M. Effects of Amantadine Binding on the Dynamics of Bilayer-Bound Influenza A M2 Transmembrane Peptide Studied by NMR Relaxation. *J Biomol NMR.* 2009; 45:185–196. [PubMed: 19633911]
62. Holsinger LJ, Lamb RA. Influenza Virus-M2 Integral Membrane-Protein Is a Homotetramer Stabilized by Formation of Disulfide Bonds. *Virology.* 1991; 183:32–43. [PubMed: 2053285]
63. Liu WL, Li H, Chen YH. N-terminus of M2 protein could induce antibodies with inhibitory activity against influenza virus replication. *FEMS Immunol Med Microbiol.* 2003; 35:141–146. [PubMed: 12628550]
64. Zebedee SL, Lamb RA. Influenza A virus M2 protein: monoclonal antibody restriction of virus growth and detection of M2 in virions. *J Virol.* 1988; 62:2762–2772. [PubMed: 2455818]
65. Cho KJ, BS, Seok JH, Kim S, Roose K, Lee JH, Gallardo R, Van Hamme E, Schymkowitz J, Rousseau F, Fiers W, Saelens X, Kim KH. Structure of the extracellular domain of matrix protein 2

- of influenza A virus in complex with a protective monoclonal antibody. *J Virol.* 2015; 89:3700–3711. [PubMed: 25609808]
66. Cho KJ, Schepens B, Moonens K, Deng L, Fiers W, Remaut H, Saelens X. Crystal Structure of the Conserved Amino Terminus of the Extracellular Domain of Matrix Protein 2 of Influenza A Virus Grippled by an Antibody. *J Virol.* 2016; 90:611–615.

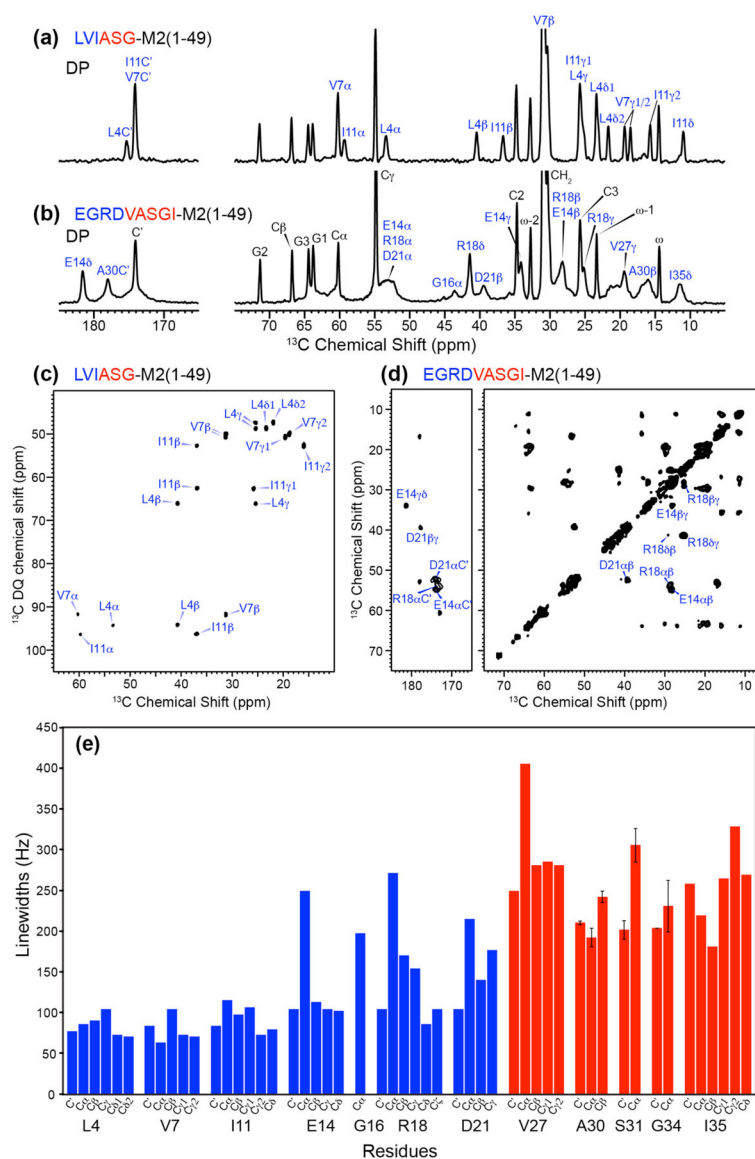
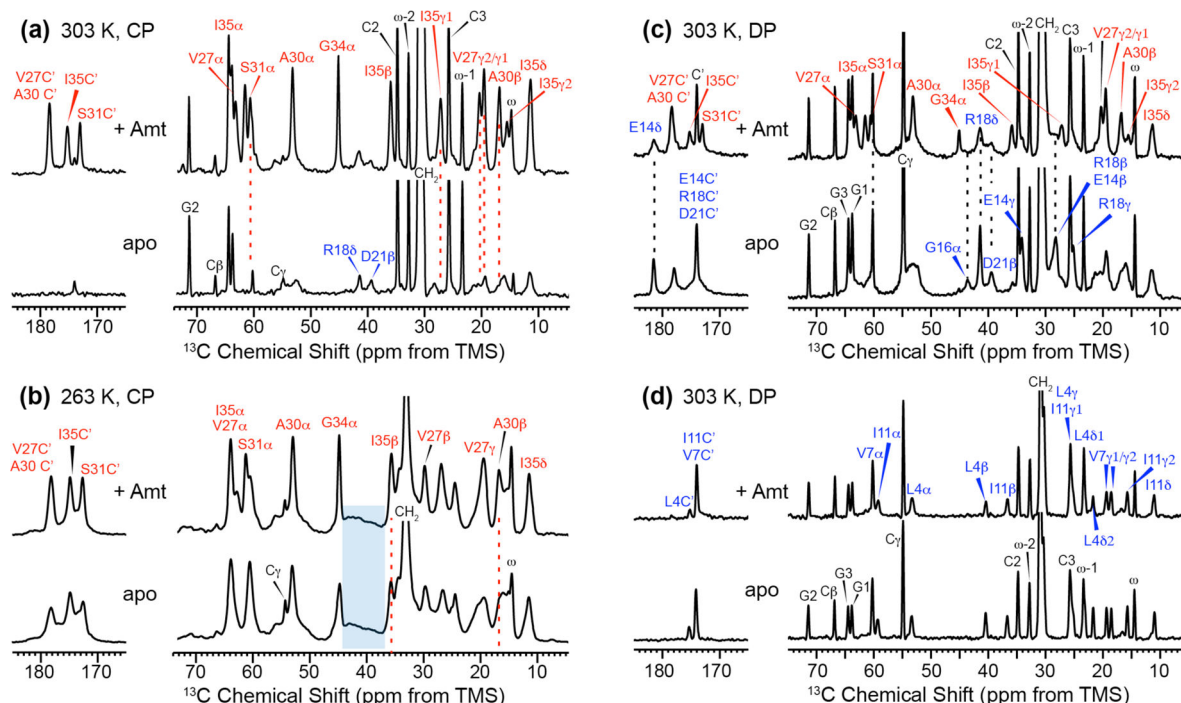
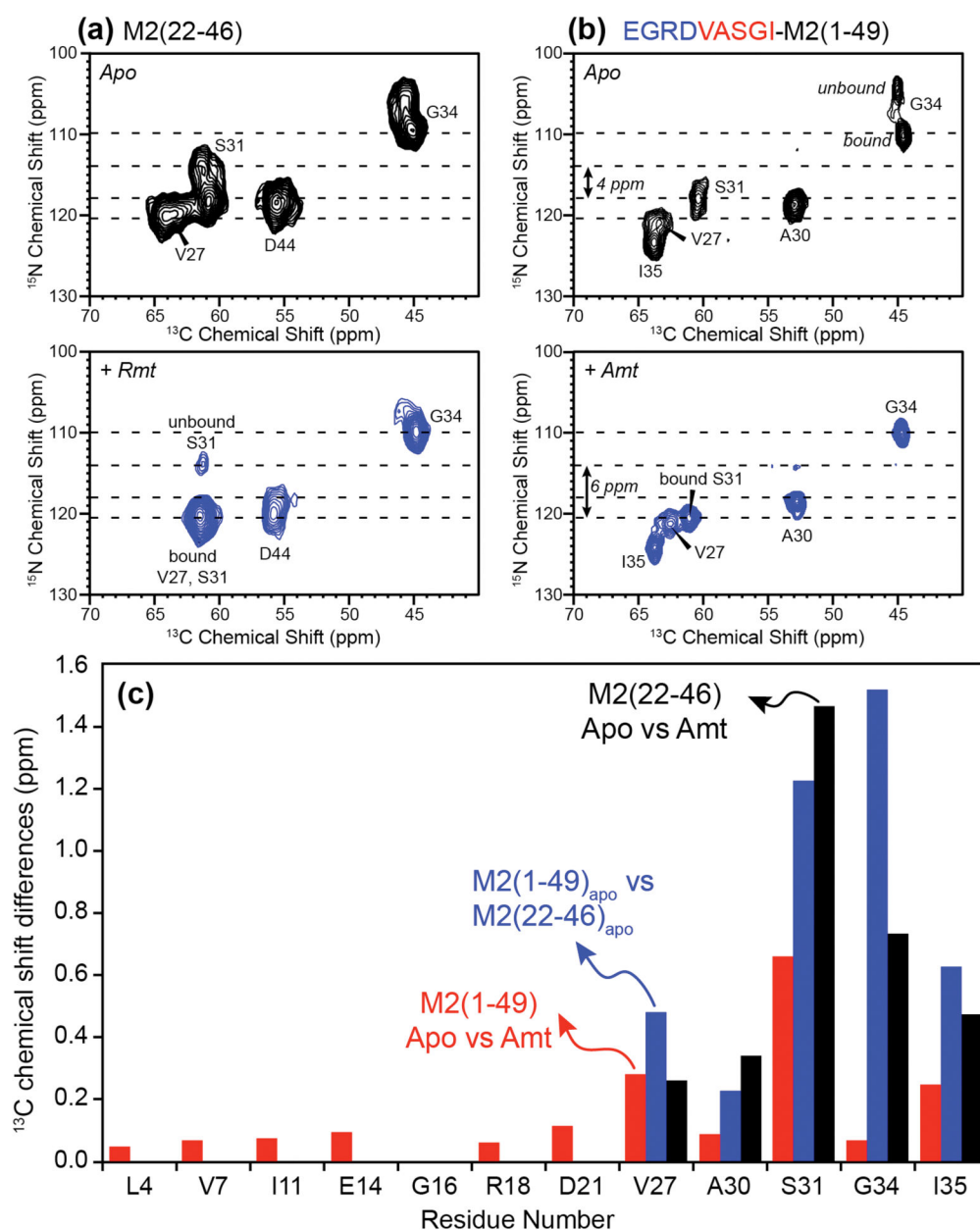


Figure 1. 1D and 2D ^{13}C spectra of DMPC-bound M2(1-49) at 303 K. (a) 1D ^{13}C DP spectrum of LVIASG-M2(1-49). (b) 1D ^{13}C DP spectrum of EGRDVASGI-M2. (c) 2D J-INADEQUATE spectrum of LVIASG-M2. (d) 100 ms 2D ^{13}C DP-DARR spectrum of EGRDVASGI-M2. The sharp signals of the ectodomain residues (assigned in blue) at random coil chemical shifts indicate the unstructured nature of the ectodomain. (e) ^{13}C full widths at half maximum of apo M2(1-49) for the labeled residues. The ectodomain linewidths are extracted from 2D INADEQUATE spectra at 303 K, while TM linewidths are extracted from 2D DARR spectra at 263 K. Note the linewidths increase from the N-terminus of the ectodomain to the TM domain.

**Figure 2.**

^{13}C MAS spectra of DMPC-bound M2(1–49) with (top row) and without (bottom row) drug (Amt). (a) ^{13}C CP spectra of EGRDVASGI-M2 at 303 K. The TM signals narrow significantly upon drug binding. (b) ^{13}C CP spectra of EGRDVASGI-M2 at 263 K. Blue shaded signals at ~40 ppm are the broadened signals of the ectodomain G16 α , R18 δ , and D21 β . (c) ^{13}C DP spectra of EGRDVASGI-M2 at 303 K. Both ectodomain and TM signals are observed. (d) ^{13}C DP spectra of LVIASG-M2 at 303 K. The ectodomain residues exhibit similar linewidths between the apo- and drug-bound states, indicating that drug binding has little effects on the local dynamics of the N-terminal residues.

**Figure 3.**

2D ^{15}N - ^{13}C correlation spectra of M2 without (top) and with (bottom) drug. (a) M2(22–46) in DMPC bilayers at 243 K³⁶. Rimantadine (Rmt), an analog of amantadine, was used to measure the drug-bound spectrum. (b) M2(1–49) in DMPC bilayers at 263 K. The ectodomain causes an S31 ^{15}N chemical shift of 118 ppm in the absence of drug. The spectra in (a) were measured on a 400 MHz spectrometer while the spectra in (b) were measured on an 900 MHz spectrometer, thus the larger linewidths in (a) reflect the lower field strength used rather than conformational heterogeneity. (c) Chemical shift differences between the apo and drug-bound M2(1–49) (red), between M2(1–49) and M2(22–46) peptides without the drug (blue bars), and between the apo and drug-bound M2(22–46). The

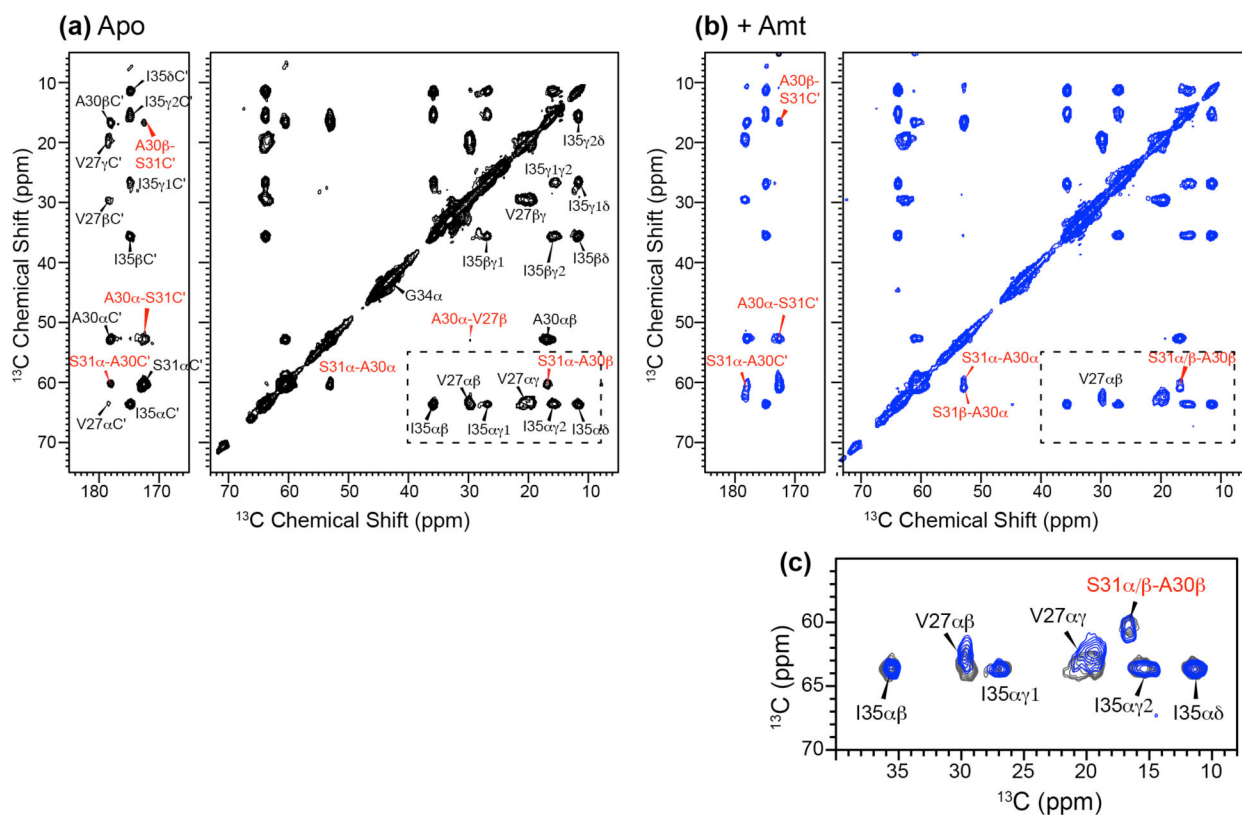
S31 chemical shift perturbation caused by the ectodomain is similar to that caused by the drug in the TM construct.

Author Manuscript

Author Manuscript

Author Manuscript

Author Manuscript

**Figure 4.**

100 ms 2D ^{13}C - ^{13}C DARR spectra of DMPC-bound EGRDVASGI-M2(1-49) without (a) and with drug (b). (c) Enlarged area of the 2D spectra showing the chemical shift perturbation to V27 caused by drug binding. Intra-residue and inter-residue cross peaks are assigned in black and red, respectively.

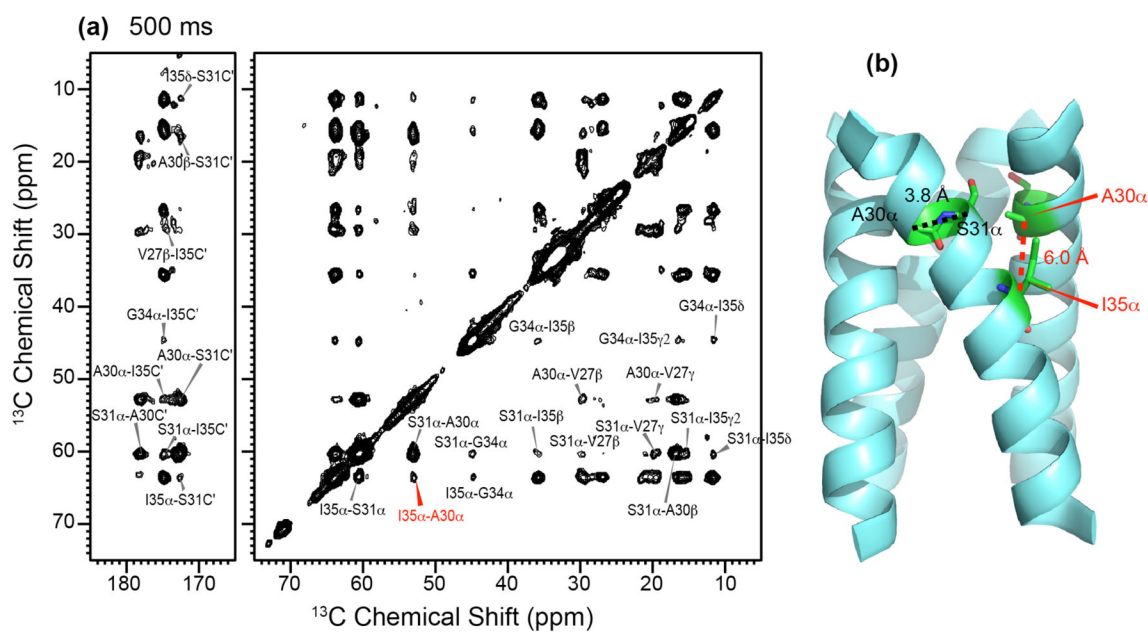


Figure 5.

(a) 500 ms 2D ^{13}C - ^{13}C correlation spectra of DMPC-bound M2(1–49). Only inter-residue cross peaks are assigned. Among these, intra-helical cross peaks are assigned in black while inter-helical cross peaks are assigned in red. (b) Crystal structure of M2(25–46) (PDB: 3LBW), showing a short inter-helical distance between A30 and I35 Ca.

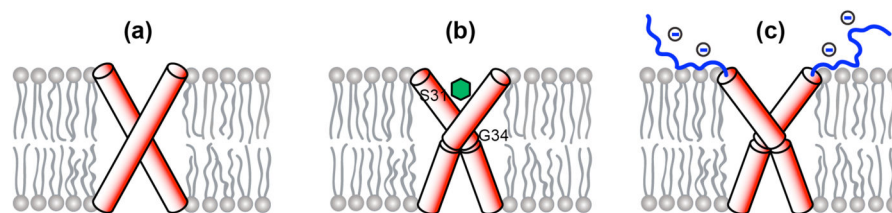


Figure 6.

Structural models of the effects of the ectodomain on the conformational equilibria of the TM helix. For clarity only two helices of the tetramer are sketched. (a) TM domain without drug. (b) TM domain with bound drug, which promotes a kink at G34. (c) The ectodomain shifts the TM domain towards the drug-bound conformation even in the absence of the drug. We attribute this conformational selection to electrostatic repulsion by the acidic residues in the ectodomain.

^{13}C and ^{15}N isotropic chemical shifts (ppm) of ectodomain and TM residues in M2(1–49) bound to DMPC bilayers. Letters s and w denote strong and weak peaks, respectively. Sites with chemical-shift differences greater than 0.5 ppm between the apo and drug-bound samples are bolded. Chemical shifts were obtained from 2D ^{13}C - ^{13}C correlation spectra, measured at 303 K and 263 K for the ectodomain and TM domain, respectively.

Table 1

Residue	State	N	CO	C α	C β	C γ 1	C γ 2	C δ 1	C δ 2	C ζ
L4	Apo	-	175.5	53.3	40.6	25.3		23.2	21.8	
	Amt	-	175.4	53.3	40.6	25.3		23.2	21.8	
V7	Apo	-	174.3	60.2	31.1	19.4	18.6			
	Amt	-	174.2	60.2	31.0	19.4	18.6			
I11	Apo	-	174.3	59.6	36.8	25.7	15.8	11.0		
	Amt	-	174.2	59.5	36.7	25.7	15.8	11.0		
E14	Apo	-	173.9	54.7	28.1	33.9		181.4		
	Amt	-	173.9	54.7	27.9	33.9		181.4		
G16	Apo	-	-	43.7						
	Amt	-	-	43.7						
R18	Apo	-	173.7	53.7	28.6	25.1		41.3		157.6
	Amt	-	173.7	53.7	28.6	25.2		41.3		157.5
D21	Apo	-	173.9	52.4	39.3	177.8				
	Amt	-	173.9	52.5	39.3	177.6				
V27	Apo	121.0	178.4	63.4	29.9	19.4	20.4			
	Amt	121.2	178.3	62.4	29.7	19.3	20.2			
A30	Apo	118.5	177.9	52.8	16.5					
	Amt	118.2	177.9	52.7	16.6					
S31	Apo	117.9s	172.3	60.3	-					
		115.4w								
	Amt	120.2	172.5	60.9	60.2					

Author Manuscript

Author Manuscript

Author Manuscript

Author Manuscript

Residue	State	N	CO	Ca	Cβ	Cγ1	Cγ2	Cδ1	Cδ2	Cξ
G34	Apo	109.9s	175.0	44.5s						
		104.5w		45.2w						
	Amt	109.9	175.0	44.6						
I35	Apo	123.4	174.8	63.9	35.6	26.8	15.8	11.1		
	Amt	124.2	174.8	63.8	35.5	26.8	15.3	11.3		

¹³C and ¹⁵N isotropic chemical shifts of TM domain in DMPC-bound M2(1–49) and DLPC-bound M2(22–46) without and with amantadine (Amt). Sites with chemical-shift differences greater than 0.5 ppm are bolded. Letters s, m, and w denote strong, medium, and weak, respectively.

Table 2

Residue	Site	M2(1–49)		M2(22–46)	
		Apo	+ Amt	Apo	+ Amt
V27	N	121.0	121.2	120.4	120.2
	CO	178.4	178.3	177.8	178.1
	Ca	63.4	62.4	63.8	63.9
					62.0
	Cβ	29.9	29.7	29.7	30.0
	Cγ1	19.4	19.3	19.3	19.5
	Cγ2	20.4	20.2	21.2	20.8
A30	N	118.5	118.2	118.0w	118.4
				119.4m	
	CO	177.9	177.9	177.7	177.5
	Ca	52.8	52.7	52.8	52.8
	Cβ	16.5	16.6	16.5	17.0
S31	N	117.9	120.2	114.7	121.4
	CO	172.3	172.5	173.7	173.1
	Ca	60.3	60.9	61.2	61.3
	Cβ	-	60.2	60.8	59.8
G34	N	109.9	109.9	107.1	109.7
		104.5			106.3
	CO	175.0	175.0	173.0	173.2s
					175.0w
	Ca	44.5s	44.6	45.7	45.0s
		45.2w			45.5w
I35	N	123.4	124.2	122.3	124.6
	CO	174.8	174.8	175.5	175.4

Author Manuscript

Author Manuscript

Author Manuscript

Author Manuscript

Residue	Site	M2(1–49)		M2(22–46)	
		Apo	+ Amt	Apo	+ Amt
	Cα	63.9	63.8	63.9	63.8
	Cβ	35.6	35.5	35.7	35.8
	Cγ1	26.8	26.8	28.1	27.3
	Cγ2	15.8	15.3	15.7	15.6
	Cδ1	11.1	11.3	11.7	11.6